BIOCHEMISTRY

An enzymatic cleavage-triggered minimally invasive nanosensor for urine-based detection of early atherosclerosis

Zhina Wu[1,2], Rui Liu[3], Jianai Chen[3], Xueying Cai[3], Jingzheng Yi[4], Jiasi Wang[5]*, Di Wang[3,6]*, Min Hu[1,2]*

Timely detection of early atherosclerosis (AS) is crucial for improving cardiovascular outcomes, creating a growing demand for diagnostic tools that are simple, sensitive, and cost-effective. Here, we introduce a synthetic nanosensor for early AS detection that leverages the fluorescence and renal clearance properties of carbon quantum dots (CQDs). This nanosensor, designed to respond to the proteolytic activity of AS-associated dysregulated enzymes, entails CQDs as signal reporters to convert AS-associated proteolytic activity to fluorometric readings enabling a sensitive and cost-effective urine-based assay for early AS detection. Our findings demonstrated that the nanosensor provided distinct signals in atherosclerotic versus healthy mice at early AS stages, indicating its diagnostic potential. Moreover, toxicity tests showed no notable adverse effects, supporting its safety for diagnostic applications. This minimally invasive diagnostic approach could facilitate personalized therapy design and continuous efficacy assessment. It is expected that such a modular nanosensor platform can be integrated with simple urine tests to offer cost-effective detection of various diseases.

INTRODUCTION

Simple, sensitive, and early disease diagnosis is crucial for enabling early intervention, improving cure rates, prolonging survival, and enhancing quality of life, in particular in developing countries and regions with high disease burdens (*1*, *2*). Cardiovascular diseases (CVDs) have a prevalence exceeding 50% with rising incidence rates, making them among the most common chronic diseases. In particular, the majority of deaths from CVDs occur in low- and middle-income countries (*3*, *4*). Atherosclerosis (AS), characterized by the accumulation of fatty plaques in the intimal layer of arteries, leads to asymmetrical focal thickening of plaques and ultimately serious cardiac issues (*5*). Early diagnosis of AS enables timely intervention, notably reducing the incidence and progression of CVDs and thus helping alleviate the global CVD burden (*6*).

Current diagnostic criteria for AS primarily rely on invasive imaging techniques, such as angiography, which provides only morphological information of advanced plaques. Moreover, the high cost of these techniques limits their widespread implementation in impoverished areas (*7*). On the other hand, AS carries a high risk but develops asymptomatically, making early diagnosis imperative. Recent studies have explored the potential for early AS diagnosis through nanomolecular imaging methods, including computed tomography (CT), magnetic resonance imaging (MRI), ultrasound imaging, photoacoustic imaging (PAI), and fluorescence imaging (*8*, *9*). Protease activity is closely linked to inflammation, thrombosis, and plaque formation. Researches indicate that matrix metalloproteinase–9 (MMP-9) levels are higher in unstable plaques, while MMP-2 levels are elevated in stable lesions (*10*, *11*). Platelet-derived MMP-2 plays a crucial role in early AS development, as circulating activated platelets, which express MMP-2 on their surface, interact with endothelial protease-activated receptor-1(PAR-1), triggering signaling pathways that lead to the exposure of adhesion molecules, such as vascular cell adhesion molecule–1 (VCAM-1). This process promotes the adhesion and migration of monocytes across the endothelial monolayer, ultimately leading to AS formation (*12*). In addition, elevated MMP-9 levels in plasma and plaque tissue have been observed in patients with symptomatic carotid artery disease (*13*). Therefore, monitoring the activity of MMP-2 and MMP-9 could serve as a functional biomarker for AS.

Traditional methods for detecting protease activity primarily involve mass spectrometry and imaging techniques, both of which are complex and require high-end equipment (*14*, *15*). For example, Han *et al.* (*16*) designed a fluorescent nanoprobe conjugated with MMP-2 aptamers, successfully visualizing atherosclerotic plaques in vitro using *ApoE*-knockout mice. Similarly, Qin *et al.* (*17*) developed an efficient PAI probe by conjugating gold nanorods with MMP-2 antibodies to target MMP-2 in atherosclerotic plaques. However, these imaging-based methods for detecting MMPs rely on specialized instruments, involve complex procedures, require skilled technicians, and are relatively costly, limiting their widespread application. Enzyme activity–based nanosensors, recently emerging as minimally invasive alternatives to traditional imaging methods that rely on contrast agents and are thus subject to low sensitivity for early disease detection, enhance early diagnosis of conditions such as liver fibrosis, thrombosis, immune rejection, and cancer (*18*–*22*).

This study presents a PEG-peptide-CQDs (polyethylene glycol–peptide–carbon quantum dots, referred to as PPCs) nanosensor conjugating two specific peptide sequences covalently. The targeted peptide is capable of specific binding to VCAM-1, enabling accumulation at the pathology site, and an enzyme-sensitive peptide substrate can be cleaved by MMP-2 and MMP-9 to release CQDs, facilitating AS diagnosis through direct urinary fluorescence detection. In this design, CQDs, which have renal-clearance capability,

[1]Department of Orthodontics, Hospital of Stomatology, Jilin University, Changchun 130021, China. [2]Jilin Provincial Key Laboratory of Tooth Development and Bone Remodeling, Changchun 130021, China. [3]School of Life Sciences, Jilin University, Changchun, Jilin 130012, China. [4]Western Dental, Fresno, CA, USA. [5]Guangdong Provincial Key Laboratory of Sensor Technology and Biomedical Instrument, School of Biomedical Engineering, Shenzhen Campus of Sun Yat-sen University, Shenzhen 518107, China. [6]Engineering Research Center of Chinese Ministry of Education for Edible and Medicinal Fungi, Jilin Agricultural University, Changchun, Jilin 130118, China.
*Corresponding author. Email: wangjs8@mail.sysu.edu.cn (J.W); jluwangdi@jlu.edu.cn (D.W); Humin@jlu.edu.cn (M.H)

fluorescent properties, and high biocompatibility, are used as signal reporter linked to a PEG carrier via an MMP-sensitive substrate peptide. At atherosclerotic lesions, the peptide is cleaved by up-regulated MMP-2 and MMP-9, releasing CQDs to be subsequently excreted into the urine, with their urinary fluorescence intensity related to total activity of the two MMPs. This enables highly sensitive early detection of AS. Furthermore, the PPCs nanosensor demonstrates a measurable response to therapeutic intervention and thus facilitates the evaluation of treatment efficacy. This urine-based, minimally invasive biomonitoring method allows for early diagnosis and therapeutic monitoring of AS without relying on complex imaging techniques. Its ease of use and high sensitivity make it suitable for broad applications in clinical diagnostics.

RESULTS

Design of PPCs nanosensor

A 40-kDa eight-arm PEG scaffold with excellent biocompatibility was used as the carrier for fabricating the PPCs nanosensor, where the PEG scaffold is linked to CQDs via a substrate peptide sensitive to both MMP-2 and MMP-9, with CQDs serving as signal reporters due to their high quantum yields, narrow emission peaks, and ease of modification (*23*). We used the eight-arm PEG as the chaperone because it is inexpensive, has minimal uptake by the reticuloendothelial system or macrophages, and thus extends the blood half-life of the cargo (*19*, *21*). Upon intravenous administration of PPCs, the substrate peptide is specifically cleaved by MMP-2 and MMP-9 at atherosclerotic lesions, releasing CQDs from the PPCs into the bloodstream. Because of their small size (<5 nm), the released CQDs are filtered by the kidneys and excreted into the urine, determined by a simple fluorometer, serving as an indicator of disease status (Fig. 1).

Feasibility of PPCs nanosensor

Trace detection and in vivo stability of CQDs

The CQDs exhibited a distinct emission spectrum with a peak at 515 nm, characterized by a narrow emission profile (Fig. 2A). In aqueous solution, the CQDs were detectable at concentrations as low as fg/ml, exhibiting a linear relationship between log(fluorescence) and log(concentration) over a range of 0.1 ng/ml to 10 μg/ml, allowing for precise quantitative analysis (fig. S1 and Fig. 2, B and C). The strong physiological and fluorescence stability of CQDs in blood and urine enables reliable, noninvasive urinary monitoring. Urine samples were collected at various time points after injection of CQDs into healthy mice. Most CQDs were excreted through the renal pathway within 1 hour of injection, with their urinary fluorescence remaining stable. This result indicates that these CQDs can circulate stably within the mouse body without interference from blood components (Fig. 2, D and E). In addition, real-time observation of the metabolism of CQDs within the mouse body was achieved through in vivo imaging, corroborating the urinary assay results (Fig. 2, F and G).

In vitro activity of peptide substrate responsive to MMP-2 and MMP-9

To confirm the responsiveness of the substrate peptide to MMP-2 and MMP-9, we synthesized a fluorogenic version of the substrate peptide by incorporating the fluorophore fluorescein and the quencher dabcyl (table S1), and then tested its hydrolysis by several

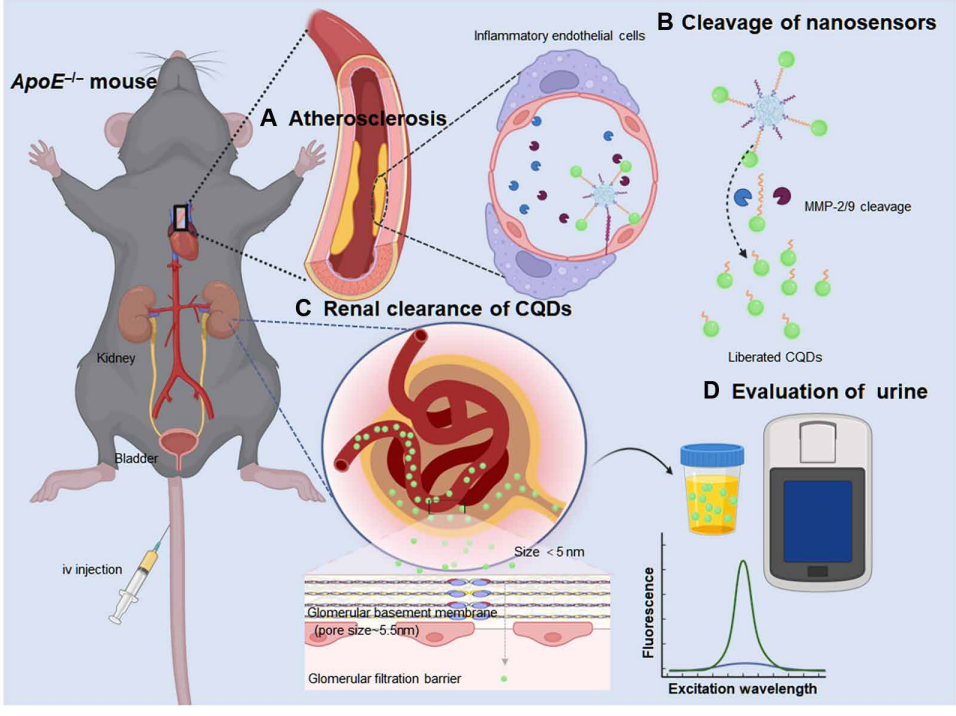

Fig. 1. Design of PPCs nanosensor for AS detection. (**A**) The PPCs nanosensor is administered via tail vein injection in *ApoE*$^{-/-}$ mice, where they will target atherosclerotic lesions in the aorta and respond to up-regulated MMP-2 and MMP-9. (**B**) The MMP-responsive module of PPCs is cleaved by MMP-2 and MMP-9, releasing CQDs into the bloodstream. (**C**) Because of their small size (<5 nm), the released CQDs are filtered through the kidneys and excreted into the urine. (**D**) The fluorescence of urinary CQDs is simply detected with a fluorometer.

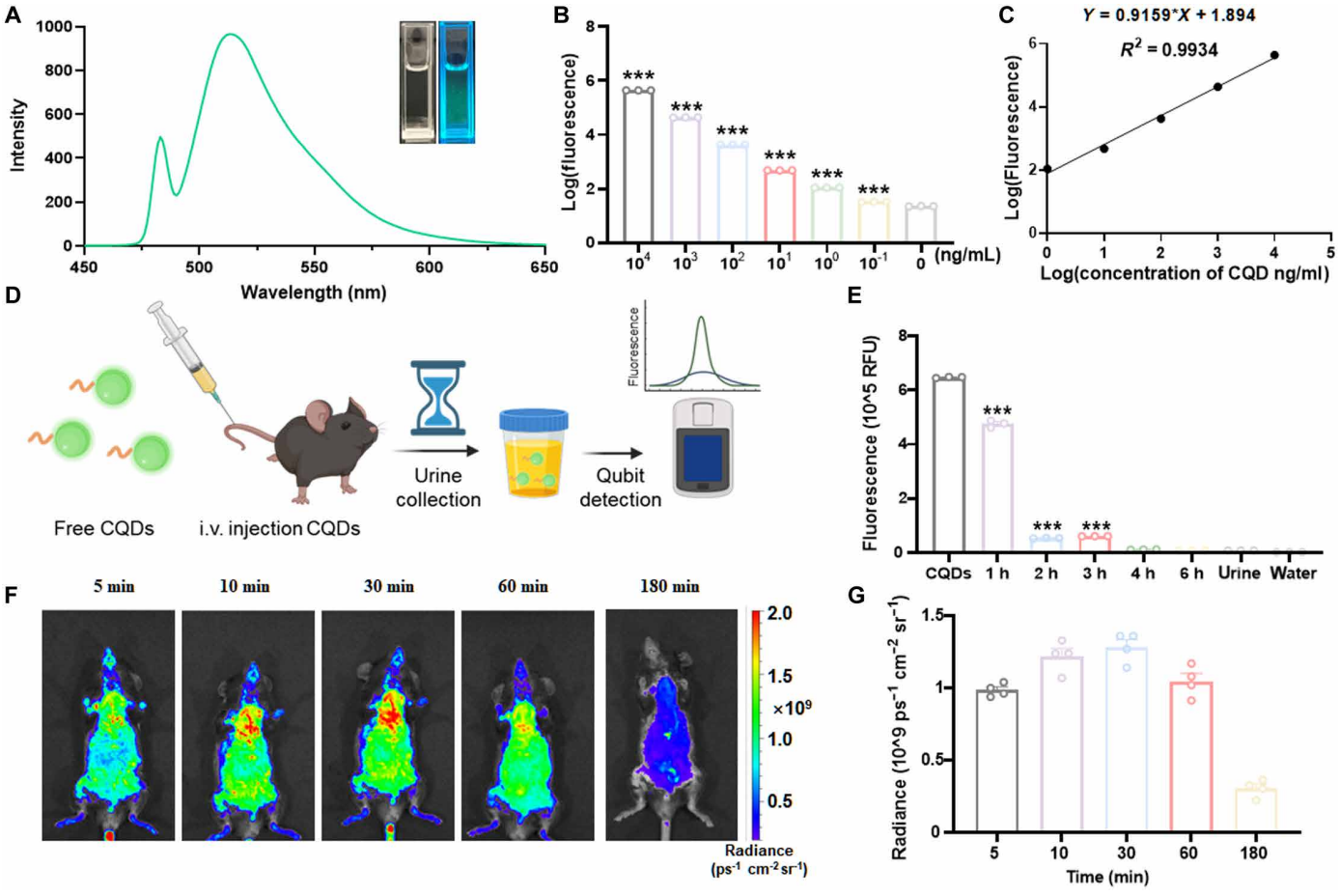

Fig. 2. Fluorescence characterization of CQDs and their renal clearance in vivo. (**A**) Fluorescence spectrum of CQDs (0.1 mg/ml); (**B** and **C**) Fluorescence intensity of CQDs at various concentrations in aqueous solution (mean ± SEM, ***$P < 0.001$, $n = 3$). (**D**) Schematic illustration of CQD renal clearance: CQDs were administered intravenously (i.v.) in C57BL/6J mice, with subsequent urine collection and fluorescence analysis at different time points. (**E**) Urinary fluorescence intensity of CQDs at various time points after injection (mean ± SEM, $n = 3$, ***$P < 0.001$). (**F**) Representative in vivo IVIS imaging and (**G**) fluorescence intensity of CQDs in healthy mice over time after injection (mean ± S.E.M., $n = 4$). RFU, relative fluorescence units.

typical proteases, MMP-2, MMP-9, Marimastat, and a blood-derived protease (thrombin). Both MMP-2 and MMP-9 cleaved the fluorogenic peptide, releasing the fluorophore without interference from serum or thrombin, while Marimastat, an MMP-2 and MMP-9 inhibitor, effectively abolished the proteolytic activity of these MMPs on this modified substrate. Neither thrombin nor serum components hydrolyzed this modified peptide (Fig. 3, A and B). Furthermore, the ability of this modified peptide to detect endogenous MMPs was validated using the culture supernatant from foam cells, a cell type associated with atherosclerotic lesions (Fig. 3C).

Characterization of PPCs and their response to MMP activity

CQDs are less than 5 nm in size, which is below the glomerular filtration cutoff size (~5.5 nm), whereas the synthesized PPCs have a size of approximately 20 nm, making them unsuitable for renal clearance (*24*, *25*) (Fig. 3D). The spectra of PPCs, with a peak approximately at near 525 nm, could be observed, like those of CQDs (fig. S2). To examine whether the conjugation of the substrate peptide to PEG affects its cleavage by MMPs and thus the release of CQDs, we performed a cleavage test by incubating PPCs with MMP-2 and MMP-9, followed by using a 10-kDa dialysis bag to separate the enzymatic cleavage products and measuring their fluorescence. A strong fluorescence signal was detected outside the dialysis bag, confirming the in vitro sensitivity of PPCs to these MMPs (Fig. 3, E and F). Furthermore, to assess the in vivo stability of PPCs and their response to MMP activity, we injected PPCs, along with MMP-2 and MMP-9, into healthy mice. Fluorescence was subsequently detected in the urine of the mice, indicating successful MMP-induced cleavage and renal excretion of CQDs (Fig. 3, G and H). These results demonstrate the stability and sensitivity of the PPCs nanosensor in response to MMP activity both in vitro and in vivo.

Biocompatibility and biodistribution of VCAM-1–targeting PPCs

AS is a chronic inflammatory disease in which endothelial cell dysfunction plays a crucial role in plaque formation and progression (*26*, *27*). Endothelial cells express VCAM-1, which serves as the primary target for nanosensor-mediated diagnosis of this vascular condition (*28*). To enable targeted detection of atherosclerotic lesions, we designed some PPCs to also include the VHPK (Val-His-Pro-Lys) peptide, which binds specifically to VCAM-1. Compared to the PPCs that were designed to not contain the VHPK peptide and thus referred to as non–VCAM-1–targeting PPCs, the VCAM-1–targeting

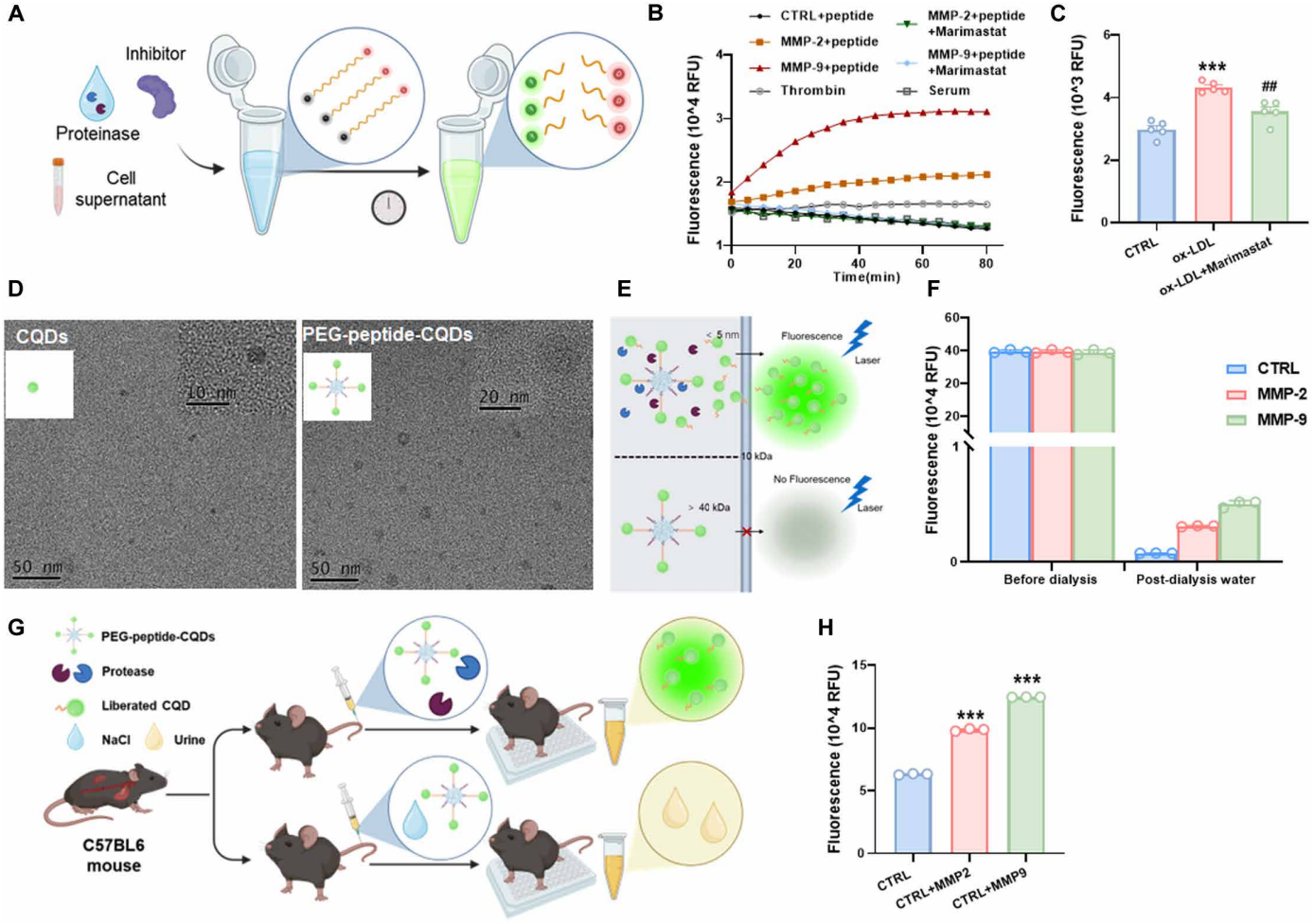

Fig. 3. Feasibility and characterization of PPCs nanosensor. (**A**) Schematic of disease-associated protease activity. (**B**) Representative activation profiles of fluorogenic substrate peptides after treatment with recombinant proteases, showing a rapid increase in fluorescence intensity for specific protease-substrate combinations (mean ± SEM, $n = 3$). (**C**) Fluorescence analysis of supernatant from foam cells treated with lipopolysaccharide (LPS; 1 μg/ml) and oxidized low-density lipoprotein (Ox-LDL; 100 μg/ml), with or without Marimastat (10 μM), followed by incubation with the substrate peptide (mean ± SEM, $n = 5$; ***$P < 0.001$ compared with CTRL group; ##$P < 0.01$ compared with Ox-LDL group). (**D**) TEM images displaying the particle size of CQDs and PPCs. (**E**) Schematic of the in vitro enzymatic cleavage of PPCs. (**F**) Fluorescence intensity of the dialysis solution before and after in vitro enzymatic cleavage of PPCs (mean ± SEM, $n = 3$). (**G**) Schematic of the in vivo enzymatic cleavage of PPCs. (**H**) Urinary fluorescence intensity in healthy mice 1 hour after PPCs administration (mean ± SEM, $n = 3$, ***$P < 0.001$).

PPCs were more localized at lesions in $ApoE^{-/-}$ mice with prolonged circulation time in vivo (Fig. 4, A to C). Furthermore, the fluorescence intensity of the aortas was notably stronger in mice injected with VCAM-1–targeting PPCs, further confirming the lesion-targeting ability of VCAM-1–targeting PPCs (Fig. 4, D and E). Before detection, we assessed the in vitro and in vivo biocompatibility of VCAM-1–targeting PPCs. The VCAM-1–targeting PPCs with a concentration of 0.1 mg/ml exhibited no measurable cytotoxicity (fig. S3). The in vivo toxicity was investigated by pathological examination of the mice following their administration (0.1 mg/ml at a volume of 0.2 ml). Compared to the control group, no observable body changes over 28 days and no histological evidence of toxicity were found in organs such as the heart, liver, lungs, spleen, and kidneys in PPCs injection group at short (1 day) or long (14 days) time points (Fig. 4F and fig. S4), indicating that VCAM-1–targeting PPCs did not induce systemic toxicity. Fluorescence imaging of major organs was further conducted to explore the distribution of VCAM-1–targeting PPCs in the body. Fluorescence signals were primarily detected in the liver and kidneys (Fig. 4G), indicating that VCAM-1–targeting PPCs were primarily cleared through hepatic and renal pathways. For simplicity, all PPCs mentioned hereafter refer to VCAM-1–targeting PPCs, unless otherwise specified.

Early disease detection and therapeutic effects monitoring

To verify the detection ability of PPCs nanosensor for early AS, blood lipid tests were conducted at 4, 6, 8, 10, and 14 weeks after initiating a high-fat diet (HFD) feeding in $ApoE^{-/-}$ mice (Fig. 5A). After 4 weeks of HFD feeding, $ApoE^{-/-}$ mice showed notably elevated serum levels of total cholesterol (TC), triglycerides (TG), and low-density lipoprotein (LDL), along with markedly reduced high-density lipoprotein (HDL) levels (fig. S5, A to D), indicative of hyperlipidemia, a form of abnormal lipid metabolism known to accelerate AS progression. Although hyperlipidemia is a well-established risk factor for AS and other CVDs, it is not a specific diagnostic marker for

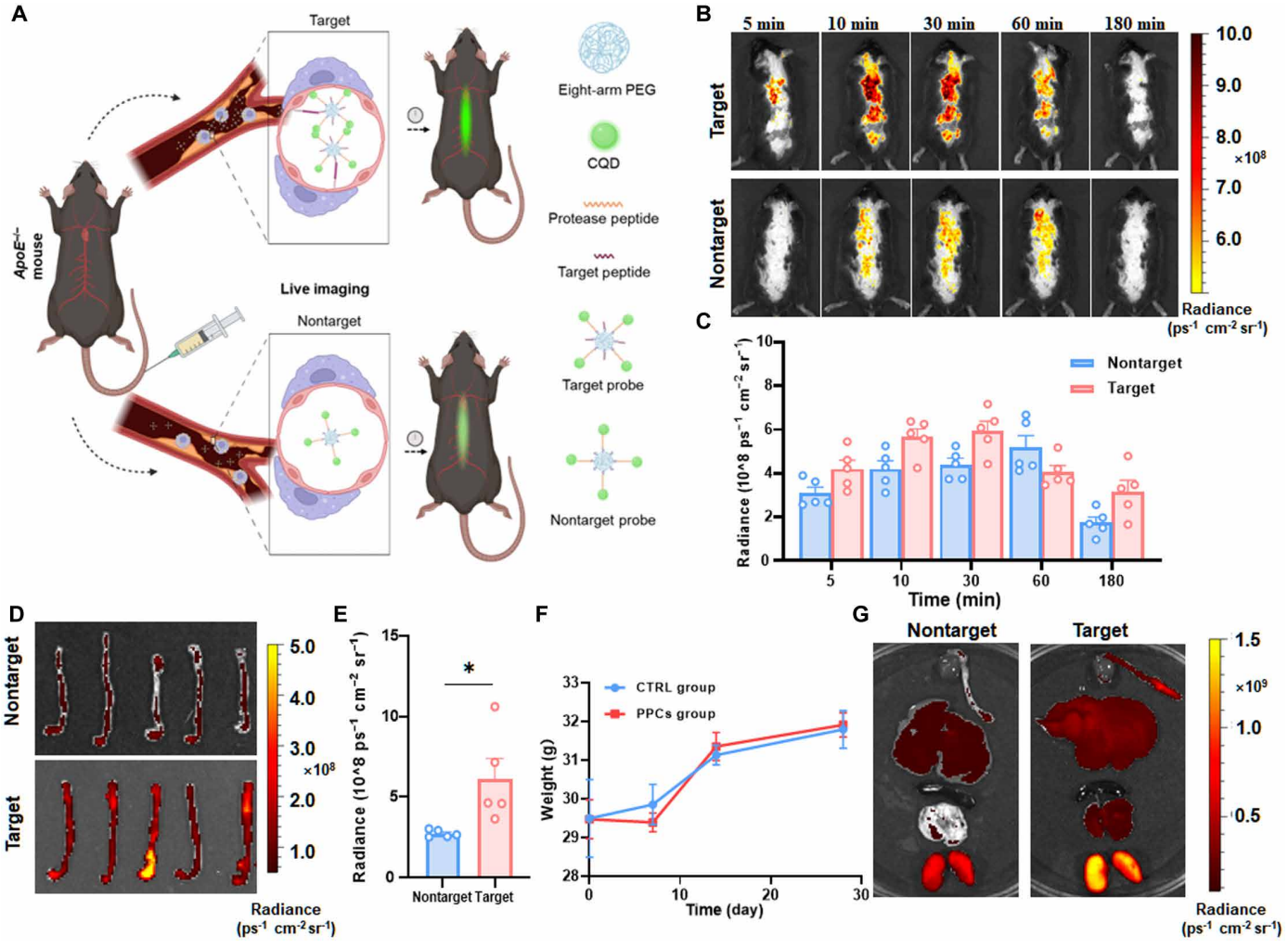

Fig. 4. Biodistribution and biocompatibility of PPCs. (**A**) Schematic of fluorescence-based detection of atherosclerotic lesions in *ApoE*$^{-/-}$ mice using VCAM-1–targeting versus nontargeting PPCs. (**B** and **C**) Representative IVIS imaging and quantification in *ApoE*$^{-/-}$ mice after administration of the two types of PPCs. (**D**) Representative IVIS imaging and (**E**) Fluorescent intensity of the aorta from the mice in (B). (**F**) Body weight changes over 28 days in the PPCs group compared to the CTRL group. (**G**) Representative IVIS imaging of major organs from the mice in (B). Data are presented as mean ± SEM ($n = 5$), *$P < 0.05$.

AS, as it is strongly influenced by dietary patterns and lifestyles. To accurately assess the progression of AS, Oil Red O staining was performed on the aorta of mice. After 6 weeks of HFD feeding, the staining revealed fatty streaks in the aorta of *ApoE*$^{-/-}$ mice, but no notable intimal thickening, suggesting that AS had progressed to stage II. At 8 weeks, notable intimal thickening and fibrous cap formation were observed, indicating progression to stages III to IV lesions (*29*, *30*). At 10 weeks and beyond, clear plaque formation was noted, with signs of erosion and even rupture, reflecting severe atherosclerotic conditions (Fig. 5B).

The tissue Western blot (WB) results were consistent with the Oil Red O staining findings. At 8 weeks, MMP-2 and MMP-9 expression levels were significantly elevated in *ApoE*$^{-/-}$ mice compared to healthy mice ($P < 0.05$; Fig. 5, C to E), supporting the role of these MMPs in the progression of atherosclerotic plaques (*31*). These findings suggest that detecting MMP-2 and MMP-9 could provide a promising approach for AS diagnosis. Enzyme-linked immunosorbent assay (ELISA) results further confirmed these findings, showing significant differences in serum concentrations of MMP-2 and MMP-9 between *ApoE*$^{-/-}$ and healthy mice after 10 weeks of HFD feeding ($P < 0.05$; Fig. 5, F and G). This indicates that atherosclerotic mice can be differentiated from healthy mice based on serum concentrations of MMP-2 and MMP-9, though only in the later stages of AS, after plaque formation. This 2-week delay in differentiation compared to tissue WB results is likely due to the lower and rapidly fluctuating plasma concentrations of blood biomarkers (*32*). Immunofluorescence (IF) results also corroborated the tissue WB findings, showing notably elevated MMP-2 and MMP-9 expression in vascular tissues at relatively early stages (Fig. 5H). Building on these results, the PPCs nanosensor was used to detect MMP-2 and MMP-9 in *ApoE*$^{-/-}$ mice, aiming to assess whether it could distinguish between atherosclerotic and healthy mice at an early stage.

The PPCs nanosensor exploits the proteolytic activity of endogenous MMPs to release CQDs, which emit fluorescence signals. Following the release of CQDs, their stronger fluorescence intensity in the urine enables highly sensitive detection of MMP-2 and MMP-9 levels. Experimental results demonstrated that the PPCs nanosensor could detect elevated MMP-2 and MMP-9 levels at disease sites in

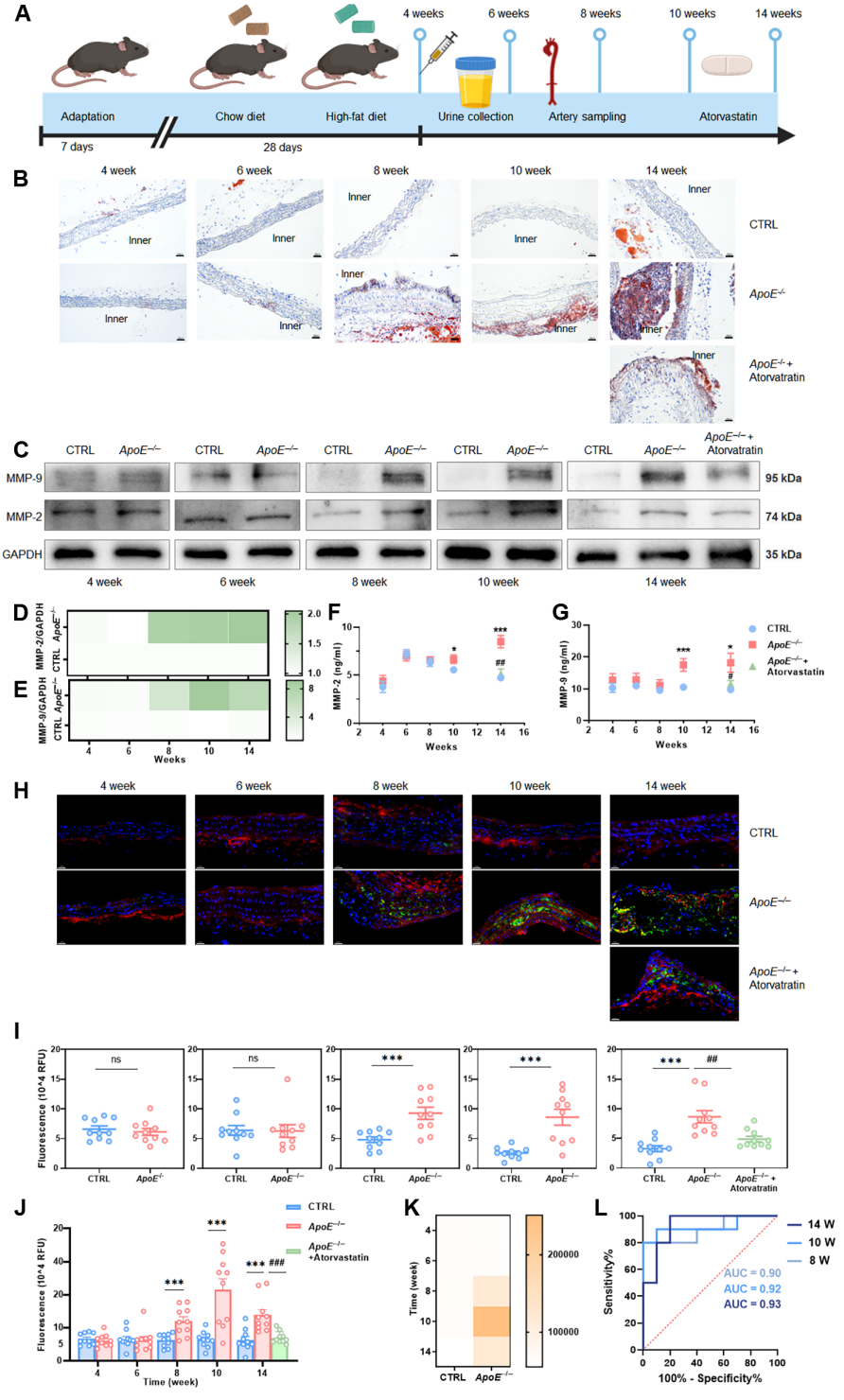

Fig. 5. The PPCs nanosensor enables early AS detection and therapeutic effect monitoring. (**A**) Timeline for AS modeling and urinary detection using the PPCs nanosensor. (**B**) Oil Red O staining of aortic tissues in healthy mice (CTRL) and *ApoE*$^{-/-}$ mice at various time points ($n = 3$; scale bars, 50 μm). (**C** to **E**) Expression levels of MMP-2 and MMP-9 in aortic tissues from healthy mice, *ApoE*$^{-/-}$ mice, and *ApoE*$^{-/-}$ mice treated with atorvastatin ($n = 3$). (**F** and **G**) Serum levels of MMP-2 and MMP-9 in healthy mice, *ApoE*$^{-/-}$ mice, and *ApoE*$^{-/-}$ mice treated with atorvastatin ($n = 10$). (**H**) Representative IF staining images showing MMP-2 (red) and MMP-9 (green) expression in aortic tissues from healthy mice, *ApoE*$^{-/-}$ mice, and *ApoE*$^{-/-}$ mice treated with atorvastatin; the nuclei are stained blue with DAPI ($n = 3$; scale bar, 20 μm). (**I** to **K**) Urinary fluorescence intensity of healthy mice, *ApoE*$^{-/-}$ mice, and *ApoE*$^{-/-}$ mice treated with atorvastatin after administration of PPCs at 4 to 14 weeks, with (**L**) corresponding ROC analysis. Data are presented as mean ± SEM ($n = 10$), with $^{*}P < 0.05$, $^{**}P < 0.01$, and $^{***}P < 0.001$ compared to CTRL mice, as well as $\#P < 0.05$ and $\#\#P < 0.01$ compared to *ApoE*$^{-/-}$ mice; ns, not significant.

ApoE$^{-/-}$ mice fed a HFD for 8 weeks. During this early stage of AS, increased MMP activity led to cleavage of the substrate peptide and release of CQDs, which were subsequently filtered through the kidneys and excreted into the urine, where they were detected using fluorescence. This enables effective differentiation between healthy and atherosclerotic mice in an early stage (Fig. 5, I to K). Furthermore, we performed receiver operating characteristic (ROC) analysis with 95% confidence intervals (CIs) to quantify the performance of PPCs on AS detection at 8, 10, and 14 weeks, which yielded areas under the curve of 0.9 (95% CI, 0.76 to 1), 0.92 (95% CI, 0.78 to 1), and 0.93 (95% CI, 0.82 to 1), respectively (Fig. 5L). The PPCs had a sensitivity of 80% (95% CI, 0.49 to 0.96) and specificity of 90% (95% CI, 0.6 to 0.99) at 8 weeks, as well as a sensitivity of 90% (95% CI, 0.6 to 0.99) and specificity of 90% (95% CI, 0.60 to 0.99) at 10 weeks, for identifying AS from healthy mice. At 14 weeks, PPCs had a sensitivity and specificity of 100% (95% CI, 0.72 to 1) and 80% (95% CI, 0.49 to 0.96), respectively, indicating that as AS progresses, the diagnostic capability of PPCs for AS improves in sensitivity. Furthermore, no notable differences in urine volume were observed between groups (fig. S6, A to E), ensuring that variations in urine volume did not notably affect the concentration of CQDs. This allows for a direct assessment of AS status based on urinary fluorescence, with fluorescence intensity serving as an accurate indicator of disease progression. To date, few studies have developed minimally invasive, imaging-independent nanosensors for diagnosing various AS stages. The PPCs nanosensor developed in this study successfully detects various AS stages, enabling early diagnosis with high sensitivity.

Regular monitoring of the efficacy of anti-AS drugs is crucial for the timely clinical assessment of disease progression and therapeutic effects. After confirming the feasibility of PPCs nanosensor for early AS detection, we used it to monitor the treatment effect of atorvastatin. After 10 weeks of HFD feeding, *ApoE*$^{-/-}$ mice were divided into two groups: one to receive atorvastatin treatment (3 mg/kg per day), while the other to receive phosphate-buffered saline (PBS) treatment as a control. After 4 weeks of treatment, histopathological analysis revealed alleviated AS progression in *ApoE*$^{-/-}$ mice treated with atorvastatin compared to the PBS-treated group (Fig. 5B), which was in agreement with decreased urinary fluorescence intensity detected by the PPCs nanosensor (Fig. 5, I and J). These results highlight the potential of PPCs nanosensor in monitoring disease progression and assessing the efficacy of therapeutic strategies.

DISCUSSION

AS, a chronic, progressive disease characterized by continued plaque progression, is a major contributor to thrombosis, cerebral infarction, myocardial infarction, and other CVDs, posing notable health risks. Early identification of AS enables effective and timely interventions, but traditional imaging-based methods rely on costly imaging equipment such as CT and MRI, and often fail to detect the disease in its early stages. In addition, diagnosing CVD in remote or poor settings remains challenging due to limited access to well-equipped clinical laboratories and trained medical personnel. Consequently, CVD has been the highest cause of mortality in the developing world, leading to severe social and economic burden (*33*). Studies have shown that the expression levels of MMP-9 and MMP-2 increase during early AS, making these proteins promising biomarkers for early AS diagnosis. In poor resource environments, AS detection should be simple to operate, built from inexpensive components, and able to detect disease directly from biological fluids.

In this work, we designed a PPCs nanosensor to detect MMPs, which sensitively indicates disease through the urinary analysis, providing a simple and low-cost method to diagnose early AS in resource-limited settings. It operates with minimal infrastructure, leveraging a substrate peptide responsive to MMP-9 and MMP-2, along with fluorescent CQDs, to monitor the proteolytic activity of AS-associated MMPs. Our findings demonstrated that the CQDs have strong physiological stability and biocompatibility, with stable fluorescent properties in vivo. To model the pathological features of AS, macrophages were exposed to oxidized LDL (Ox-LDL) and lipopolysaccharide (LPS), which induced foam cells with elevated expression levels of MMP-9 and MMP-2. These MMPs efficiently cleaved the fluorogenic substrates. This demonstrates that the substrate peptide specifically interacts with AS-associated MMPs, underscoring its high importance for AS detection.

VCAM-1 is overexpressed in inflamed vascular endothelial cells, making it an ideal target for detecting atherosclerotic lesions. The PPCs nanosensor includes the VHPK peptide, which specifically binds to VCAM-1, enabling VCAM-1–targeting PPCs to accumulate more rapidly at the lesions, with the accumulation peaking at 30 min. This efficient accumulation allows for faster cleavage of PPCs at the lesions, thereby enhancing the detection efficiency for AS. Our results demonstrated that the PPCs nanosensor notably outperformed blood biomarkers in diagnostic efficiency in a mouse model of AS, achieving a diagnostic accuracy of over 90%. This high diagnostic accuracy is crucial for early AS detection and intervention, which are in turn key to risk stratification and achieving favorable postintervention outcomes. While most diagnostic methods for AS in mouse models focus on detection after 12 weeks of HFD feeding (*34*, *35*), we initiated diagnostic testing at various AS stages. As demonstrated by the testing, the PPCs nanosensor enables minimally invasive diagnosis at an early stage of 4 weeks in advanced of previous reported method (*34*, *35*), offering other options for diagnostic techniques. Moreover, the PPCs nanosensor has shown promise in facilitating the integration of early diagnosis, intervention, and therapeutic effect monitoring, which could contribute to reducing CVD-associated mortality. Current AS detection relies heavily on imaging-based methods, which are constrained by the high cost and complexity of the instruments, severely limiting their widespread application. In contrast, the PPCs nanosensor offers a cost-effective and user-friendly alternative, enabling immediate and sensitive AS detection with a simple fluorometer compared with currently used diagnostic methods (Table 1).

Synthetic biomarkers are emerging and have been applied to urinary detection of diseases including cancer, organ injury, allograft rejection, and infections. The design of PPCs expands the range of biomarkers and diseases detectable through urinalysis to now including AS. Compared with previous synthetic biomarker studies (table S2), this work uses CQDs as signal molecules, taking advantage of their strong fluorescence properties and low cost to enable simultaneous fluorescence imaging in vivo and in vitro. This approach allows for simple, convenient and inexpensive urinary detection. Intravenous administration is minimally invasive, while alternative delivery

Table 1. Comparison of PPCs with currently used diagnostic methods. PET, positron emission tomography; IVUS, intravascular ultrasound; OCT, optical coherence tomography; NIRS, near-infrared spectroscopy.

Methods	Strengths	Limitations	Ref
CT imaging	High resolution; short time; low cost	Poor sensitivity; lack of specificity; radiation	(*8*, *41*)
MR imaging	High sensitivity; minimally invasive; radiation-free; high resolution; superior tissue contract	Long time; artifact; toxicity	(*8*, *42*)
PET imaging	Superior sensitivity; short time	Limited spatial resolution; radiation; high cost	(*42*, *43*)
IVUS imaging	High resolution	Limited specificity; artifacts; invasive; costliness	(*42*, *44*)
OCT imaging	Noninvasiveness; rapid scanning speed; high resolution	High cost; high operation demands; invasive	(*42*, *45*)
NIRS	Noninvasive	Nonspecific; limited tissue penetration	(*46*, *47*)
This work	High sensitivity; minimally invasive; short time; low cost	Limited specificity	

method, including oral, inhalation, and subcutaneous injection, have also been developed, simplifying the administration process.

Nonetheless, PPCs has limitations, the most notable being limited specificity. Disease heterogeneity, interpatient variation, and comorbidities in the human population contribute to variations in MMP expression among individuals, which can result in failure to detect AS. Differences in hydration status, disease models, kidney function and complications among patients can affect urine volume and signal intensity. In addition, MMPs dysregulation occurs in other diseases, and while combining additional biomarkers or using multiplexed sensor designs could improve diagnostic specificity, it often comes at the expense of complex synthesis and procedures unsuitable for scaled-up industrial production (*36*). To further enhance accessibility, administration routes should be simplified, such as through oral, inhalation, transdermal delivery, facilitating follow-up, and reducing the need for frequent hospital visits. This approach could help lower both direct health care costs and indirect costs, such as productivity.

Although this work has shown success in preclinical studies, several translational challenges remain, including long-term biosafety, scalability, and uniform regulatory protocols (*37*). First, notable physiological differences between mice and humans must be considered, in particular in areas such as in vivo circulation, retention in issues, whole-body distribution, and clearance. These factors require further investigation in clinical trials, and the inclusion of more representative animal models should be prioritized (*38*). Second, scalability is a critical factor for successful translation. Key features influencing scalability including effectiveness, reproducibility, compatibility, sustainability, clarity, and adaptability, all of which warrant further study (*39*). Successful clinical implementation also requires standardization across multiple aspects of the technology, such as device fabrication, sterilization and packaging, sample collection, and storage and testing procedures (*37*). Standards of effectiveness have yet to be fully established, emphasizing the need for additional preclinical studies and clinical trials to guide the development of regulatory policies.

In summary, we have developed a synthetic biomarker responsive to MMP-2 and MMP-9 for early and rapid AS detection. This method entails simple, rapid, and sensitive urinary fluorescence measurement to enable immediate detection, allowing for timely AS diagnosis. Unlike traditional imaging tools and imaging-based nanoscale diagnostic techniques (*40*), the PPCs nanosensor does not require complex detection processes or specialized imaging instruments. Instead, it offers advantages such as low invasiveness, affordability, and ease of operation. In addition, the PPC nanosensor has shown promise in monitoring disease progression, providing a timely and cost-effective tool for therapeutic effect assessment. By modifying the sequences of substrate peptides to be cleaved by specific enzymes, a family of nanosensors could be developed to monitor various diseases and guide therapeutic decisions, especially in low-resource settings.

MATERIALS AND METHODS

Reagents

Unless otherwise specified, all reagents were used without additional purification. CQDs (10 mg/ml) were purchased from Suzhou Xingshuo Nanotech Co. Ltd. (Suzhou, China). Peptides and ELISA kits were obtained from Sangon Biotech Co. Ltd. (Shanghai, China). The eight-arm PEG-MAL (40 kDa) was sourced from JenKem Technology Co. Ltd. (Beijing, China), and Ox-LDL (YB-002) was purchased from Yiyuan Biotechnologies (Guangzhou, China). LPS (L8880) and 1-ethyl-3-[3-(dimethylamino) propyl] carbodiimide (EDC·HCl) were supplied by Beijing Solarbio Science & Technology Co. Ltd. (Beijing, China). Marimastat was obtained from MedChemexpress (Shanghai, China). SnakeSkin dialysis tubing (10,000 molecular weight cutoff) and horseradish peroxidase–conjugated anti-rabbit or anti-mouse immunoglobulin G (IgG) were acquired from Thermo Fisher Scientific (MA, USA). MMP-2 (902-MP) and MMP-9 (911-MP) were sourced from R&D Systems (MN, USA), and thrombin was obtained from Sigma-Aldrich (MA, USA). TC, TG, LDL, and HDL assay kits were all purchased from Nanjing Jiancheng Bioengineering Institute (Nanjing, China). Radioimmunoprecipitation assay (RIPA) lysis buffer was obtained from Millipore (20-188; MA, USA). Protease and phosphatase inhibitors (P002) were supplied by NCM Biotech (Suzhou, China), and MMP-2 (AF5330) and MMP-9 (AF5228) antibodies were obtained from Affinity Biosciences (OH, USA). The ECL chemiluminescence kit (K1231) was purchased from APExBIO (TX, USA), polyvinylidene fluoride membranes (0.45 μm) were sourced from Cytiva (MA, USA), and rapid closure solution was obtained from Genefist (GF1815; Beijing, China). The Oil Red O kit was obtained from BaiQianDu Biotechnology (Wuhan, China).

Instruments

Fluorescence spectra were measured with a Shimadzu spectrofluorophotometer (RF-5301PC) to characterize the emission profile of the CQDs and PPCs, while an Invitrogen Qubit 4 fluorometer was used for sensitive fluorescence detection and quantification in urine.

Transmission electron microscopy (TEM) images were obtained using a Hitachi HT-7000 transmission electron microscope. Fluorescence images were captured with the IVIS Spectrum imaging system (PerkinElmer). Fluorescence intensity was recorded using a Biotek Synergy Neo2 microplate reader, and absorbance measurements were taken with a Biotek Synergy HT microplate reader. A chemiluminescence image analysis system (Tanon 5200; Shanghai, China) was used to detect protein signals. A freezing microtome (Thermo Fisher Scientific) was used for tissue sectioning.

Detection and quantification of CQDs

CQDs (10 mg/ml) were diluted in a gradient with PBS. Their fluorescence intensity was measured using the Invitrogen Qubit 4 fluorometer.

Urinary detection of CQDs

All animal studies were conducted in accordance with the guidelines set by the Jilin Committee of Use and Care of Laboratory Animals, and the project protocols were approved by the Animal Ethics Committee of Jilin University (approval no. SY202409028). Male C57BL/6J and *ApoE*$^{-/-}$ mice (6 to 8 weeks old) were obtained from Jiangsu Huachuang Xinnuo Pharmaceutical Technology Co. Ltd. [SCXK(Su)2020-0009, Jiangsu, China].

The detection limit of CQDs in urine was determined using the Invitrogen Qubit 4 fluorometer. Male C57BL/6J mice (8 weeks old) were administered CQDs (0.1 mg/ml, 200 μl) via tail vein injection, and their urine was collected at specified time points for fluorescence measurement. The mice were placed in custom-built housing with a 96-well plate base to facilitate urine collection.

In vivo metabolism of CQDs

To investigate the in vivo metabolism, healthy male C57BL/6J mice (8 weeks old) were administered CQDs (0.1 mg/ml, 200 μl) via tail vein injection and then imaged using the IVIS system (excitation filter, 500 nm; and emission filter, 540 nm).

Validation of the substrate peptide of MMP-2/9

A peptide substrate modified with a fluorophore and quencher was designed to validate the cleavage ability of MMP-2 and MMP-9. The fluorogenic substrate peptide (0.2 mg/ml, 50 μl) was incubated with serum (10%), thrombin, and MMP-2 or MMP-9 (0.2 μg/ml, 50 μl), with or without Marimastat (10 μM, final concentration), and the fluorescence intensity was monitored in real time using a fluorescence microplate reader to assess enzymatic cleavage.

J774A.1 cells, obtained from the American Type Culture Collection, were cultured in Dulbecco's modified Eagle's medium with 10% fetal bovine serum under a 5% humidified CO_2 atmosphere at 37°C. To induce foam cells, J774A.1 cells were incubated with Ox-LDL (100 μg/ml, final concentration) and LPS (1 μg/ml, final concentration) for 24 hours. Next, the cell culture supernatant was collected and then coincubated with the fluorogenic substrate peptide for 1 hour, followed by measuring fluorescence intensity with a Qubit 4 fluorometer to evaluate enzymatic cleavage. In the assay to inhibit foam cell formation, Marimastat (10 μM, final concentration) was cocultured with Ox-LDL (100 μg/ml, final concentration), LPS (1 μg/ml, final concentration), and J774A.1 cells for 24 hours.

Synthesis of PPCs

A PEG-peptide conjugate was synthesized via a thiol-maleimide reaction. The substrate peptide, targeting peptide, and eight-armed PEG were mixed at a molar ratio of 5:3:1 (18 mg:5 mg:80 mg, in 2.5 ml PBS, pH = 7.4), and incubated at room temperature for 1 hour. CQDs (10 mg/ml) were activated with EDC (25-mg CQDs with 50-mg EDC) in the dark for 1 hour. Next, the PEG-peptide conjugate and activated CQDs were mixed at a ratio of 1:1 in volume (2.5-ml PEG-peptide and 2.5-ml activated CQDs) and incubated overnight in the dark to synthesize PPCs. Dialysis tubing (10 kDa) was conducted to remove free CQDs. The fluorescence intensity of free CQDs was determined using a Qubit 4 fluorometer, followed by diluting the solution to 0.1 mg/ml for further use.

Characterization of PPCs and their in vitro cleavage

TEM was used to observe the morphological features and sizes of PPCs. The fluorescence spectroscopy of PPCs and free CQDs has been performed using a spectrofluorophotometer.

To investigate in vitro enzymatic cleavage, PPCs were incubated with MMP-2 and MMP-9 (0.1 μg/ml final concentration) separately, followed by dialysis tubing (10 kDa) to separate the released CQDs. The cleavage of PPCs by MMP-2 and MMP-9 was evaluated by measuring the fluorescence intensity of the dialysis fluid.

In vivo cleavage of PPCs

To validate whether PPCs can be cleaved by enzymes in vivo, PPCs (0.1 mg/ml, 200 μl) were injected into healthy C57BL/6J mice via the tail veins along with PBS, MMP-2, or MMP-9 (0.1 μg/ml, 100 μl). Urine samples were collected 1 hour postinjection, followed by fluorescence intensity measurement with a Qubit 4 fluorometer.

In vitro and in vivo toxicity studies

The viability of J774A.1 cells was assessed using the methyl thiazolyl tetrazolium (MTT) assay. Cells (5×10^4/ml) were seeded in a 96-well plate and treated with PPCs (0.1 mg/ml) for 24 hours. MTT (20 μl, 5 mg/ml) was added to the plate and incubated for 4 hours. The absorbance at a wavelength of 520 nm was measured, and cell viability was expressed as a percentage of the control group. Healthy C57BL/6 mice were administered PPCs (0.1 mg/ml, 200 μl) via tail vein injection compared with the PBS-injected control mice. Main organs were harvested at 1 and 28 days postinjection. Heart, liver, spleen, lung, and kidney tissues were fixed and stained with hematoxylin and eosin to analyze in vivo toxicity.

Targeting performance and in vivo metabolism of PPCs

To establish an AS model, *ApoE*$^{-/-}$ mice were fed a HFD (60% fat, 20% carbohydrates, 20% protein, Xiaoshu Youtai, Beijing) for 12 weeks. Peptide-modified, targeting and nontargeting PPCs (0.1 mg/ml, 200 μl) were injected separately into the tail veins of atherosclerotic mice, followed by fluorescence imaging as described above. After treatment with PPCs, mice were euthanized and perfused with PBS (pH 7.4). The aorta and organs (heart, liver, spleen, lungs, and kidneys) were extracted and rinsed three times with PBS (pH 7.4), followed by fluorescence imaging of these organs using the methods described above.

Early AS detection

PPCs (0.1 mg/ml, 200 μl) were administered via tail vein injection to both healthy and atherosclerotic mice. Mice were placed in custom-built housing with a 96-well plate base. Urine samples were collected 1 hour postinjection and analyzed using a Qubit 4 fluorometer. AS progression was monitored after 4, 6, 8, 10, and 14 weeks of HFD feeding to assess the ability of PPCs to detect AS at early stages.

Therapeutic effect monitoring

To monitor therapeutic effects, $ApoE^{-/-}$ mice fed a HFD for 10 weeks were randomly divided into two groups ($n = 10$ per group), including an intragastrically HFD-fed group with normal saline (5 ml/kg), an intragastrically atorvastatin (3 mg/kg; Lipitor, Pfizer Ireland Pharmaceuticals)–treated group daily for 4 weeks. Healthy mice administered normal saline served as the control group. After 4 weeks, disease status was monitored using the PPCs nanosensor.

Lipid testing

Peripheral blood was obtained by sampling from the retro-orbital venous plexus. Serum was collected twice by centrifugation at 3500 rpm at 4°C for 10 min. TG, TC, LDL-C, and HDL-C assay kits were used to determine lipid levels in the serum samples.

Oil Red O staining and IF staining

Aortic tissues were fixed in 4% paraformaldehyde for 24 hours, and then dehydrated in 15 and 30% sucrose solutions at 4°C. The tissues were embedded, sectioned at 10 μm, incubated in Oil Red O solution for 8 to 10 min at room temperature, rinsed with water, and counterstained with hematoxylin for 3 to 5 min at room temperature. After a final water rinse, the tissue sections were coated with glycogelatin and observed under a microscope. For IF, antigens were retrieved after frozen sectioning, blocked with 3% bovine serum albumin for 30 min, incubated with the primary antibody overnight at 4°C, washed three times with PBS, and then incubated with the secondary antibody at room temperature in the dark for 50 min. Following three PBS washes, the sections were stained with 4′,6-diamidino-2-phenylindole (DAPI) solution at room temperature in the dark for 10 min. Slides were coated with Multi Mount 480 and observed under a fluorescence microscope.

ELISA assay for serum MMP-2 and MMP-9

Serum MMP-2 and MMP-9 levels were measured using the ELISA assay kits.

WB analysis

Total protein was extracted from aortic tissue samples using RIPA lysis buffer with protease and phosphatase inhibitors, and then quantified using the BCA method. Furthermore, 40 μg of total protein was separated on 10% SDS–polyacrylamide gel electrophoresis and transferred to polyvinylidene fluoride membranes. The membranes were blocked at 25°C for 15 min with rapid closure solution, and then incubated with primary antibodies at 4°C for 10 to 12 hours, followed by incubation with horseradish peroxidase–conjugated anti-rabbit or anti-mouse IgG (31460 or 31430) at 4°C for 4 hours. Protein signals were detected using an ECL chemiluminescent substrate detection kit with a chemiluminescence image analysis system and semi-quantified using ImageJ software.

Supplementary Materials

This PDF file includes:

Figs. S1 to S6
Tables S1 and S2
References

REFERENCES AND NOTES

1. M. Ilgar, N. Dağ, C. Türkoğlu, Importance of incidental coronary artery calcification in early diagnosis of obstructive coronary artery disease. *Pol. J. Radiol.* **88**, e338–e342 (2023).
2. K. Whitaker, Earlier diagnosis: The importance of cancer symptoms. *Lancet Oncol.* **21**, 6–8 (2020).
3. K. E. Joynt Maddox, M. S. V. Elkind, H. J. Aparicio, Y. Commodore-Mensah, S. D. de Ferranti, W. N. Dowd, A. F. Hernandez, O. Khavjou, E. D. Michos, L. Palaniappan, J. Penko, R. Poudel, V. L. Roger, D. S. Kazi, Forecasting the burden of cardiovascular disease and stroke in the United States through 2050—Prevalence of risk factors and disease: A presidential advisory from the American Heart Association. *Circulation* **150**, e65–e88 (2024).
4. C. P. Benziger, G. A. Roth, A. E. Moran, The global burden of disease study and the preventable burden of NCD. *Glob. Heart* **11**, 393–397 (2016).
5. G. K. Hansson, Inflammation, atherosclerosis, and coronary artery disease. *N. Engl. J. Med.* **352**, 1685–1695 (2005).
6. X. Bao, Y. Mao, G. Si, L. Kang, B. Xu, N. Gu, Iron oxide nanoparticles: A promising approach for diagnosis and treatment of cardiovascular diseases. *Nano Res.* **16**, 12453–12470 (2023).
7. A. J. Nelson, M. Ardissino, P. J. Psaltis, Current approach to the diagnosis of atherosclerotic coronary artery disease: More questions than answers. *Ther. Adv. Chronic Dis.* **10**, 2040622319884819 (2019).
8. Y. Liu, Z. Jiang, X. Yang, Y. Wang, B. Yang, Q. Fu, Engineering nanoplatforms for theranostics of atherosclerotic plaques. *Adv. Healthc. Mater.* **13**, e2303612 (2024).
9. Y. Yang, J. Pan, A. Wang, Y. Ma, Y. Liu, W. Jiang, A novel method for the diagnosis of atherosclerosis based on nanotechnology. *J. Mater. Chem. B* **12**, 9144–9154 (2024).
10. J. P. G. Sluijter, W. P. C. Pulskens, A. H. Schoneveld, E. Velema, C. F. Strijder, F. Moll, J.-P. de Vries, J. Verheijen, R. Hanemaaijer, D. P. V. de Kleijn, G. Pasterkamp, Matrix metalloproteinase 2 is associated with stable and matrix metalloproteinases 8 and 9 with vulnerable carotid atherosclerotic lesions: A study in human endarterectomy specimen pointing to a role for different extracellular matrix metalloproteinase inducer glycosylation forms. *Stroke* **37**, 235–239 (2006).
11. Q. Xiong, Z. Wang, Y. Yu, Y. Wen, R. Suguro, Y. Mao, Y. Z. Zhu, Hydrogen sulfide stabilizes atherosclerotic plaques in apolipoprotein E knockout mice. *Pharmacol. Res.* **144**, 90–98 (2019).
12. S. Momi, E. Falcinelli, E. Petito, G. C. Taranta, A. Ossoli, P. Gresele, Matrix metalloproteinase-2 on activated platelets triggers endothelial PAR-1 initiating atherosclerosis. *Eur. Heart J.* **43**, 504–514 (2022).
13. C. Tan, Y. Liu, W. Li, F. Deng, X. Liu, X. Wang, Y. Gui, L. Qin, C. Hu, L. Chen, Associations of matrix metalloproteinase-9 and monocyte chemoattractant protein-1 concentrations with carotid atherosclerosis, based on measurements of plaque and intima-media thickness. *Atherosclerosis* **232**, 199–203 (2014).
14. D. Yepes, V. Costina, L. R. Pilz, R. Hofheinz, M. Neumaier, P. Findeisen, Multiplex profiling of tumor-associated proteolytic activity in serum of colorectal cancer patients. *Proteomics Clin. Appl.* **8**, 308–316 (2014).
15. J. S. Choi, S. Kim, D. Yoo, T. H. Shin, H. Kim, M. D. Gomes, S. H. Kim, A. Pines, J. Cheon, Distance-dependent magnetic resonance tuning as a versatile MRI sensing platform for biological targets. *Nat. Mater.* **16**, 537–542 (2017).
16. M. E. Han, S. Baek, H. J. Kim, J. H. Lee, S. H. Ryu, S. O. Oh, Development of an aptamer-conjugated fluorescent nanoprobe for MMP2. *Nanoscale Res. Lett.* **9**, 104 (2014).
17. H. Qin, Y. Zhao, J. Zhang, X. Pan, S. Yang, D. Xing, Inflammation-targeted gold nanorods for intravascular photoacoustic imaging detection of matrix metalloproteinase-2 (MMP_2) in atherosclerotic plaques. *Nanomedicine* **12**, 1765–1774 (2016).
18. J. D. Kirkpatrick, A. P. Soleimany, J. S. Dudani, H. J. Liu, H. C. Lam, C. Priolo, E. P. Henske, S. N. Bhatia, Protease activity sensors enable real-time treatment response monitoring in lymphangioleiomyomatosis. *Eur. Respir. J.* **59**, 2100664 (2022).
19. J. S. Dudani, C. G. Buss, R. T. K. Akana, G. A. Kwong, S. N. Bhatia, Sustained-release synthetic biomarkers for monitoring thrombosis and inflammation using point-of-care compatible readouts. *Adv. Funct. Mater.* **26**, 2919–2928 (2016).
20. S.-J. Liu, K. Ma, L.-S. Liu, K. Wang, Y.-A. Zhang, Z.-R. Bi, Y.-X. Chen, K.-Z. Chen, C.-X. Wang, S.-L. Qiao, Point-of-care non-invasive enzyme-cleavable nanosensors for acute transplant rejection detection. *Biosens. Bioelectron.* **215**, 114568 (2022).
21. L. Hao, R. T. Zhao, N. L. Welch, E. K. W. Tan, Q. Zhong, N. S. Harzallah, C. Ngambenjawong, H. Ko, H. E. Fleming, P. C. Sabeti, S. N. Bhatia, CRISPR-Cas-amplified urinary biomarkers for multiplexed and portable cancer diagnostics. *Nat. Nanotechnol.* **18**, 798–807 (2023).
22. C. Xu, M. Xu, Y. Hu, J. Liu, P. Cheng, Z. Zeng, K. Pu, Ingestible artificial urinary biomarker probes for urine test of gastrointestinal cancer. *Adv. Mater.* **36**, e2314084 (2024).
23. P. Devi, S. Saini, K. H. Kim, The advanced role of carbon quantum dots in nanomedical applications. *Biosens. Bioelectron.* **141**, 111158 (2019).
24. H. S. Choi, W. Liu, P. Misra, E. Tanaka, J. P. Zimmer, B. I. Ipe, M. G. Bawendi, J. V. Frangioni, Renal clearance of quantum dots. *Nat. Biotechnol.* **25**, 1165–1170 (2007).
25. B. Du, M. Yu, J. Zheng, Transport and interactions of nanoparticles in the kidneys. *Nat. Rev. Mater.* **3**, 358–374 (2018).
26. P. Libby, P. M. Ridker, G. K. Hansson, Progress and challenges in translating the biology of atherosclerosis. *Nature* **473**, 317–325 (2011).
27. P. Libby, Inflammation during the life cycle of the atherosclerotic plaque. *Cardiovasc. Res.* **117**, 2525–2536 (2021).

28. X. Zhang, F. Centurion, A. Misra, S. Patel, Z. Gu, Molecularly targeted nanomedicine enabled by inorganic nanoparticles for atherosclerosis diagnosis and treatment. *Adv. Drug Deliv. Rev.* **194**, 114709 (2023).
29. H. C. Stary, A. B. Chandler, S. Glagov, J. R. Guyton, W. Insull Jr., M. E. Rosenfeld, S. A. Schaffer, C. J. Schwartz, W. D. Wagner, R. W. Wissler, A definition of initial, fatty streak, and intermediate lesions of atherosclerosis. A report from the Committee on Vascular Lesions of the Council on Arteriosclerosis, American Heart Association. *Circulation* **89**, 2462–2478 (1994).
30. R. Virmani, F. D. Kolodgie, A. P. Burke, A. Farb, S. M. Schwartz, Lessons from sudden coronary death: A comprehensive morphological classification scheme for atherosclerotic lesions. *Arterioscler. Thromb. Vasc. Biol.* **20**, 1262–1275 (2000).
31. V. A. Myasoedova, D. A. Chistiakov, A. V. Grechko, A. N. Orekhov, Matrix metalloproteinases in pro-atherosclerotic arterial remodeling. *J. Mol. Cell. Cardiol.* **123**, 159–167 (2018).
32. J. Amiral, Measurement of blood activation markers applied to the early diagnosis of cardiovascular alterations. *Expert Rev. Mol. Diagn.* **20**, 85–98 (2020).
33. D. Yach, C. Hawkes, C. L. Gould, K. J. Hofman, The global burden of chronic diseases: Overcoming impediments to prevention and control. *JAMA* **291**, 2616–2622 (2004).
34. B. Wang, F. Yuan, S. Wang, R. Duan, W. X. Ren, J. T. Hou, Detection of atherosclerosis-associated HOCl using a mitochondria-targeted fluorescent probe. *Sens. Actuators B Chem.* **348**, 130695 (2021).
35. Z. Ye, M. Ji, K. Wu, J. Yang, A.-A. Liu, W. Sun, D. Ding, D. Liu, In-sequence high-specificity dual-reporter unlocking of fluorescent probe enables the precise identification of atherosclerotic plaques. *Angew. Chem. Int. Ed. Engl.* **61**, e202204518 (2022).
36. C. Xu, K. Pu, Artificial urinary biomarker probes for diagnosis. *Nat. Rev. Bioeng.* **2**, 425–441 (2024).
37. M. A. Younis, H. M. Tawfeek, A. A. H. Abdellatif, J. A. Abdel-Aleem, H. Harashima, Clinical translation of nanomedicines: Challenges, opportunities, and keys. *Adv. Drug Deliv. Rev.* **181**, 114083 (2022).
38. R. Jin, X. Fu, Y. Pu, S. Fu, H. Liang, L. Yang, Y. Nie, H. Ai, Clinical translational barriers against nanoparticle-based imaging agents. *Adv. Drug Deliv. Rev.* **191**, 114587 (2022).
39. A. B. Charif, H. T. V. Zomahoun, A. Gogovor, M. A. Samri, J. Massougbodji, L. Wolfenden, J. Ploeg, M. Zwarenstein, A. J. Milat, N. Rheault, Y. M. Ousseine, J. Salerno, M. Markle-Reid, F. Légaré, Tools for assessing the scalability of innovations in health: A systematic review. *Health Res. Policy Syst.* **20**, 34 (2022).
40. A. V. Poznyak, V. N. Sukhorukov, I. I. Eremin, I. I. Nadelyaeva, A. N. Orekhov, Diagnostics of atherosclerosis: Overview of the existing methods. *Front. Cardiovasc. Med.* **10**, 1134097 (2023).
41. Q. Wang, T. Wang, C. Lio, X. Yu, X. Chen, L. Liu, Y. Wu, H. Huang, L. Qing, P. Luo, Surface hydrolysis-designed AuNPs-zwitterionic-glucose as a novel tool for targeting macrophage visualization and delivery into infarcted hearts. *J. Control. Release* **356**, 678–690 (2023).
42. L. E. Mantella, K. Liblik, A. M. Johri, Vascular imaging of atherosclerosis: Strengths and weaknesses. *Atherosclerosis* **319**, 42–50 (2021).
43. P. Joseph, A. Tawakol, Imaging atherosclerosis with positron emission tomography. *Eur. Heart J.* **37**, 2974–2980 (2016).
44. H. M. Garcia-Garcia, M. A. Costa, P. W. Serruys, Imaging of coronary atherosclerosis: Intravascular ultrasound. *Eur. Heart J.* **31**, 2456–2469 (2010).
45. R. Takeshige, H. Otake, H. Kawamori, T. Toba, Y. Nagano, Y. Tsukiyama, K. I. Yanaka, H. Yamamoto, A. Nagasawa, H. Onishi, Y. Sugizaki, S. Nakano, Y. Matsuoka, K. Tanimura, K. I. Hirata, Progression from normal vessel wall to atherosclerotic plaque: Lessons from an optical coherence tomography study with follow-up of over 5 years. *Heart Vessels* **37**, 1–11 (2022).
46. S. Sanon, T. Dao, V. P. Sanon, R. Chilton, Imaging of vulnerable plaques using near-infrared spectroscopy for risk stratification of atherosclerosis. *Curr. Atheroscler. Rep.* **15**, 304 (2013).
47. X. Luo, J. Shi, R. Wang, L. Cao, Y. Gao, J. Wang, M. Hong, X. Sun, Y. Zhang, Near-infrared persistent luminescence nanoprobe for early detection of atherosclerotic plaque. *ACS Nano* **18**, 6500–6512 (2024).
48. Q. Xu, Y. Pan, X. Liu, Y. Gao, X. Luan, F. Zeng, D. Zhou, W. Long, Y. Wang, Y. Song, Hypoxia-responsive platinum supernanoparticles for urinary microfluidic monitoring of tumors. *Angew. Chem. Int. Ed. Engl.* **61**, e202114239 (2022).
49. D. Zhou, Z. Zhang, L. Pan, Y. Wang, J. Yang, Y. Gao, Y. Song, Sucrose-powered liposome nanosensors for urinary glucometer-based monitoring of cancer. *Angew. Chem. Int. Ed. Engl.* **63**, e202404493 (2024).
50. F. Wang, N. Sun, Q. Li, J. Yang, X. Yang, D. Liu, Self-referenced synthetic urinary biomarker for quantitative monitoring of cancer development. *J. Am. Chem. Soc.* **145**, 919–928 (2023).
51. S. He, J. Li, Y. Lyu, J. Huang, K. Pu, Near-infrared fluorescent macromolecular reporters for real-time imaging and urinalysis of cancer immunotherapy. *J. Am. Chem. Soc.* **142**, 7075–7082 (2020).
52. S. He, P. Cheng, K. Pu, Activatable near-infrared probes for the detection of specific populations of tumour-infiltrating leukocytes in vivo and in urine. *Nat. Biomed. Eng.* **7**, 281–297 (2023).
53. A. D. Warren, G. A. Kwong, D. K. Wood, K. Y. Lin, S. N. Bhatia, Point-of-care diagnostics for noncommunicable diseases using synthetic urinary biomarkers and paper microfluidics. *Proc. Natl. Acad. Sci. U.S.A.* **111**, 3671–3676 (2014).
54. C. N. Loynachan, A. P. Soleimany, J. S. Dudani, Y. Lin, A. Najer, A. Bekdemir, Q. Chen, S. N. Bhatia, M. M. Stevens, Renal clearable catalytic gold nanoclusters for in vivo disease monitoring. *Nat. Nanotechnol.* **14**, 883–890 (2019).
55. Q. D. Mac, A. Sivakumar, H. Phuengkham, C. Xu, J. R. Bowen, F. Y. Su, S. Z. Stentz, H. Sim, A. M. Harris, T. T. Li, P. Qiu, G. A. Kwong, Urinary detection of early responses to checkpoint blockade and of resistance to it via protease-cleaved antibody-conjugated sensors. *Nat. Biomed. Eng.* **6**, 310–324 (2022).
56. T. Danino, A. Prindle, G. A. Kwong, M. Skalak, H. Li, K. Allen, J. Hasty, S. N. Bhatia, Programmable probiotics for detection of cancer in urine. *Sci. Transl. Med.* **7**, 289ra284 (2015).
57. J. Huang, X. Chen, Y. Jiang, C. Zhang, S. He, H. Wang, K. Pu, Renal clearable polyfluorophore nanosensors for early diagnosis of cancer and allograft rejection. *Nat. Mater.* **21**, 598–607 (2022).
58. J. D. Kirkpatrick, A. D. Warren, A. P. Soleimany, P. M. K. Westcott, J. C. Voog, C. Martin-Alonso, H. E. Fleming, T. Tammela, T. Jacks, S. N. Bhatia, Urinary detection of lung cancer in mice via noninvasive pulmonary protease profiling. *Sci. Transl. Med.* **12**, eaaw0262 (2020).
59. J. S. Dudani, M. Ibrahim, J. Kirkpatrick, A. D. Warren, S. N. Bhatia, Classification of prostate cancer using a protease activity nanosensor library. *Proc. Natl. Acad. Sci. U.S.A.* **115**, 8954–8959 (2018).
60. J. Huang, Y. Jiang, J. Li, S. He, J. Huang, K. Pu, A renal-clearable macromolecular reporter for near-infrared fluorescence imaging of bladder cancer. *Angew. Chem. Int. Ed. Engl.* **59**, 4415–4420 (2020).
61. B. Du, Y. Chong, X. Jiang, M. Yu, U. G. Lo, A. Dang, Y. A. Chen, S. Li, E. Hernandez, J. C. Lin, J. T. Hsieh, J. Zheng, Hyperfluorescence imaging of kidney cancer enabled by renal secretion pathway dependent efflux transport. *Angew. Chem. Int. Ed. Engl.* **60**, 351–359 (2021).
62. D. Zhou, Y. Yin, Z. Zhu, Y. Gao, J. Yang, Y. Pan, Y. Song, Orally administered platinum nanomarkers for urinary monitoring of inflammatory bowel disease. *ACS Nano* **16**, 18503–18514 (2022).
63. B. Ruan, M. Yu, Y. Zhou, W. Xu, Y. Liu, B. Liu, L. Zhu, S. Yi, Y. Jiang, J. Huang, Size-transformable superoxide-triggered nanoreporters for crosstalk-free dual fluorescence/chemiluminescence imaging and urinalysis in living mice. *Angew. Chem. Int. Ed. Engl.* **62**, e202305812 (2023).
64. K. Y. Lin, G. A. Kwong, A. D. Warren, D. K. Wood, S. N. Bhatia, Nanoparticles that sense thrombin activity as synthetic urinary biomarkers of thrombosis. *ACS Nano* **7**, 9001–9009 (2013).
65. P. Tempst, Mass-encoded, synthetic biomarkers and multiplexed urinary monitoring: New frontiers in disease monitoring. *Clin. Chem.* **59**, 1694–1695 (2013).
66. X. Song, M. Li, S. Ni, K. Yang, S. Li, R. Li, W. Zheng, D. Tu, X. Chen, H. Yang, Ultrasensitive urinary diagnosis of organ injuries using time-resolved luminescent lanthanide nano-bioprobes. *Nano Lett.* **23**, 1878–1887 (2023).
67. Y. Chen, P. Pei, Z. Lei, X. Zhang, D. Yin, F. Zhang, A promising NIR-II fluorescent sensor for peptide-mediated long-term monitoring of kidney dysfunction. *Angew. Chem. Int. Ed. Engl.* **60**, 15809–15815 (2021).
68. J. Weng, Y. Wang, Y. Zhang, D. Ye, An activatable near-infrared fluorescence probe for in vivo imaging of acute kidney injury by targeting phosphatidylserine and caspase-3. *J. Am. Chem. Soc.* **143**, 18294–18304 (2021).
69. F. Ding, S. Zhang, S. Liu, J. Feng, J. Li, Q. Li, Z. Ge, X. Zuo, C. Fan, Q. Xia, Molecular visualization of early-stage acute kidney injury with a DNA framework nanodevice. *Adv. Sci.* **9**, e2105947 (2022).
70. J. Huang, J. Li, Y. Lyu, Q. Miao, K. Pu, Molecular optical imaging probes for early diagnosis of drug-induced acute kidney injury. *Nat. Mater.* **18**, 1133–1143 (2019).
71. J. Huang, C. Xie, X. Zhang, Y. Jiang, J. Li, Q. Fan, K. Pu, Renal-clearable molecular semiconductor for second near-infrared fluorescence imaging of kidney dysfunction. *Angew. Chem. Int. Ed. Engl.* **58**, 15120–15127 (2019).
72. J. Huang, Y. Lyu, J. Li, P. Cheng, Y. Jiang, K. Pu, A renal-clearable duplex optical reporter for real-time imaging of contrast-induced acute kidney injury. *Angew. Chem. Int. Ed. Engl.* **58**, 17796–17804 (2019).
73. P. Cheng, W. Chen, S. Li, S. He, Q. Miao, K. Pu, Fluoro-photoacoustic polymeric renal reporter for real-time dual imaging of acute kidney injury. *Adv. Mater.* **32**, e1908530 (2020).
74. J. Huang, J. Huang, P. Cheng, Y. Jiang, K. Pu, Near-infrared chemiluminescent reporters for in vivo imaging of reactive oxygen and nitrogen species in kidneys. *Adv. Funct. Mater.* **30**, 2003628 (2020).

75. Q. D. Mac, D. V. Mathews, J. A. Kahla, C. M. Stoffers, O. M. Delmas, B. A. Holt, A. B. Adams, G. A. Kwong, Non-invasive early detection of acute transplant rejection via nanosensors of granzyme B activity. *Nat. Biomed. Eng.* **3**, 281–291 (2019).
76. Y. Chen, P. Pei, Y. Yang, H. Zhang, F. Zhang, Noninvasive early diagnosis of allograft rejection by a granzyme B protease responsive NIR-II bioimaging nanosensor. *Angew. Chem. Int. Ed. Engl.* **62**, e202301696 (2023).
77. P. Cheng, R. Wang, S. He, P. Yan, H. Huang, J. Chen, J. Shen, K. Pu, Artificial urinary biomarkers for early diagnosis of acute renal allograft rejection. *Angew. Chem. Int. Ed. Engl.* **62**, e202306539 (2023).
78. M. Anahtar, L. W. Chan, H. Ko, A. Rao, A. P. Soleimany, P. Khatri, S. N. Bhatia, Host protease activity classifies pneumonia etiology. *Proc. Natl. Acad. Sci. U.S.A.* **119**, e2121778119 (2022).

Acknowledgments: We acknowledge TopEdit LLC for the linguistic editing and proofreading during the preparation of this manuscript. **Funding:** This work was supported by the Jilin Province Development and Reform Commission no. 2024C011-3 (M.H.), National Natural Science Foundation of China 82470987 (M.H.), National Natural Science Foundation of China 82170994 (M.H.), "Medicine+X" Interdisciplinary Innovation Project of Jilin University no. 2024JBGS07 (M.H.), and Graduate Innovation Fund of Jilin University (Z.W.). **Author contributions:** Conceptualization: Z.W., J.W., D.W., and M.H. Methodology: Z.W., R.L., and J.C. Software: Z.W. Validation: Z.W., R.L., J.W., and D.W. Formal analysis: Z.W. Investigation: Z.W., R.L., and J.C. Resources: J.W., D.W., and M.H. Data curation: Z.W., J.W., and D.W. Visualization: Z.W., J.Y. Supervision: J.W., DW., and M.H. Project administration: Z.W., J.W., D.W., and M.H. Funding acquisition: J.W., D.W., and M.H. Writing–original draft: Z.W., R.L., X.C., and J.Y. Writing–review and editing: Z.W., R.L., J.W., D.W., and M.H. **Competing interests:** The authors declare that they have no competing interests. **Data and materials availability:** All data needed to evaluate the conclusions in the paper are present in the paper and/or the Supplementary Materials.

Submitted 21 November 2024
Accepted 10 February 2025
Published 14 March 2025
10.1126/sciadv.adu7614